Analyzing Vortex Winds in Radar-Observed Tornadic Mesocyclones for Nowcast Applications

QIN XU

NOAA/National Severe Storms Laboratory, Norman, Oklahoma

LI WEI AND KANG NAI

Cooperative Institute for Mesoscale Meteorological Studies, University of Oklahoma, Norman, Oklahoma

(Manuscript received 1 April 2015, in final form 1 July 2015)

ABSTRACT

A computationally efficient method is developed to analyze the vortex wind fields of radar-observed mesocyclones. The method has the following features. (i) The analysis is performed in a nested domain over the mesocyclone area on a selected tilt of radar low-elevation scan. (ii) The background error correlation function is formulated with a desired vortex-flow dependence in the cylindrical coordinates cocentered with the mesocyclone. (iii) The square root of the background error covariance matrix is derived analytically to precondition the cost function and thus enhance the computational efficiency. Using this method, the vortex wind analysis can be performed efficiently either in a stand-alone fashion or as an additional step of targeted finescale analysis in the existing radar wind analysis system developed for nowcast applications. The effectiveness and performance of the method are demonstrated by examples of analyzed wind fields for the tornadic mesocyclones observed by operational Doppler radars in Oklahoma on 24 May 2011 and 20 May 2013.

1. Introduction

Detecting and tracking mesocyclones from Doppler radial-velocity fields are very important processes for tornado-related severe weather warning operations, but the tasks involved often present enormous difficulties especially when mesocyclones are poorly resolved in the far radial ranges or confused with other signatures or data artifacts (such as noisy or improperly dealiased velocities) in radial-velocity fields. To overcome the difficulties, various automated mesocyclone detection methods and algorithms have been developed by many investigators (Stumpf et al. 1998; Smith and Elmore 2004; Liu et al. 2007; Newman et al. 2013; Miller et al. 2013). These methods rely on the assumption that a mesocyclone is behaving as a Rankine vortex and identify it as an object with no attempt to diagnose the detailed vortex wind field. By using a modified Rankine vortex model in combination with a uniform flow, a linear shear flow, and a linear divergence flow, Potvin et al. (2009, 2011) developed a technique for detecting mesocyclones and other convective vortices from multiple-Doppler observations and retrieving their size, strength, and translational velocity, but not the detailed vortex wind fields. To diagnose the full storm wind field, Gao et al. (2013) adapted a real-time three-dimensional variational data assimilation (3DVAR) system and showed the value of the wind field assimilated from multiple-Doppler radar data. This 3DVAR system compares favorably with the methods described above with regard to identifying storm-scale midlevel circulations, but the circulation may not be fully resolved because of the isotropic univariant background covariance used for each velocity component in the cost function. It is possible to improve the mesocyclone wind analysis by formulating vortex-flow-dependent background error correlation functions in cylindrical coordinates cocentered with the mesocyclone. This approach will be explored in this paper to develop a new method for mesocyclone wind analyses. The method can be used either in a stand-alone fashion or can be incorporated into the radar wind analysis system (RWAS; Xu et al. 2015) and performed as an additional step of targeted finescale wind analysis in the RWAS for nowcast applications.

Corresponding author address: Qin Xu, National Severe Storms Laboratory, 120 David L. Boren Blvd., Norman, OK 73072-7326. E-mail: qin.xu@noaa.gov

DOI: 10.1175/WAF-D-15-0046.1

The paper is organized as follows. The RWAS is briefly reviewed in the next section. The method for mesocyclone wind analyses is developed in section 3. The effectiveness and satisfactory performances of the method are demonstrated by illustrative examples in section 4. Conclusions follow in section 5.

2. Review of the RWAS

The initial version of RWAS was developed as a stand-alone system (without using any model-predicted background wind field) to retrieve real-time vector wind field data from single-Doppler radial-velocity observations at each selected vertical level or each selected tilt of radar scan superimposed on the radar reflectivity or radial-velocity image for nowcasting applications. This version of RWAS was evaluated for driving atmospheric dispersion models (Fast et al. 2008; Newsom et al. 2014) and implemented for operational test runs with atmospheric dispersion models. To monitor hazardous wind conditions, surface wind observations from the Oklahoma Mesonet have also been used in addition to radar radial velocities in the RWAS.

The RWAS contains a radial-velocity data quality control (QC) package to preprocess the raw data before the vector wind analysis. The QC package was recently upgraded with the newly developed algorithms to correct aliased velocities over areas threatened by intense mesocyclones and their generated tornados (Xu et al. 2013). The vector wind analysis in the RWAS uses the statistical interpolation (Daley 1991) to retrieve the horizontal vector wind field from radar radial velocities after QC. The vector wind analysis was also upgraded recently with extended capabilities to analyze radial-velocity observations from multiple radars with a model-predicted background wind field. In particular, high-resolution radial-velocity observations from multiple radars are combined into two (or three) batches of superobservations with the observation resolution coarsened to match the effective resolution of the analysis (i.e., about one-third of the decorrelation length of the background error correlation function used in the analysis) for each batch, so the observation resolution redundancy can be reduced to improve the computational efficiency (Xu 2011; Xu and Wei 2011). After this, the analysis is performed incrementally in multiple steps for different types of observations (from coarse to fine resolution) to cover and resolve different scales (from the synoptic to storm scale). For the mesocyclone vortex wind analysis presented in section 4a of this paper, the upgraded RWAS will be used to produce the mesoscale wind field by performing the following three steps:

1) A vertical profile of vector wind $\mathbf{v}$ = (zonal component u, meridional component v) is produced by the velocity–azimuth display (VAD) method as a by-product of the VAD-based dealiasing (Xu et al. 2011, 2013) for each radar, and then the VAD winds are analyzed into the background wind field using the method of statistic interpolation described in section 3.1 of Xu et al. (2015). The background wind field is extracted from the nearest forecasts from the operational Rapid Refresh (RAP) model (http://rapidrefresh.noaa.gov/) by interpolating the predicted wind fields in time and space onto the analysis grid in a $800 \times 800 \times 10\,\text{km}^3$ domain centered at the Twin Lakes, Oklahoma, Weather Surveillance Radar-1988 Doppler (KTLX). The analysis grid has a horizontal grid spacing of 10 km and contains 41 levels from the surface level ($z = 10\,\text{m}$) to $z = 10\,\text{km}$ above the ground.
2) The wind field produced in step 1 is used as background to analyze surface wind observations (at $z = 10\,\text{m}$) from the Oklahoma Mesonet employing the method described in section 3.2 of Xu et al. (2015).
3) The wind field produced in step 2 is used as background to analyze radar radial-velocity superobservations generated [using the method in section 3.2 of Lu et al. (2011)] in three batches with the observation resolutions coarsened to 30, 21, and 13 km (in both the radial and azimuthal directions), respectively, over the far radial range ($r > 80\,\text{km}$), the middle radial range ($40 < r \leq 80\,\text{km}$), and the near radial range ($r \leq 40\,\text{km}$) from each radar. The analysis method is the same as described in section 3.3 of Xu et al. (2015) but is applied serially to the above three batches of superobservations. The background error decorrelation length (or depth) is reduced consecutively to 25 (or 2), 18 (or 1), and 11 (or 0.3) km when the analysis is performed with the first, second, and third batch, respectively.

Figure 1a shows the background wind field from the operational RAP forecast. Figure 1b shows the analyzed wind field produced by the RWAS using radial velocities scanned from five operational radars plus Oklahoma Mesonet wind data around 2211 UTC for the tornadic storm on 24 May 2011. In comparison with the background winds in Fig. 1a, the analyzed winds in Fig. 1b are adjusted toward radar-observed radial winds in and around the areas covered by radar radial-velocity observations, but the adjustments are too coarse and too smooth to resolve the mesocyclone (marked by the small yellow circle).

The existing RWAS is clearly unable to resolve the mesocyclone. This inability is tied up with the following two limitations. First, the effective resolution of the

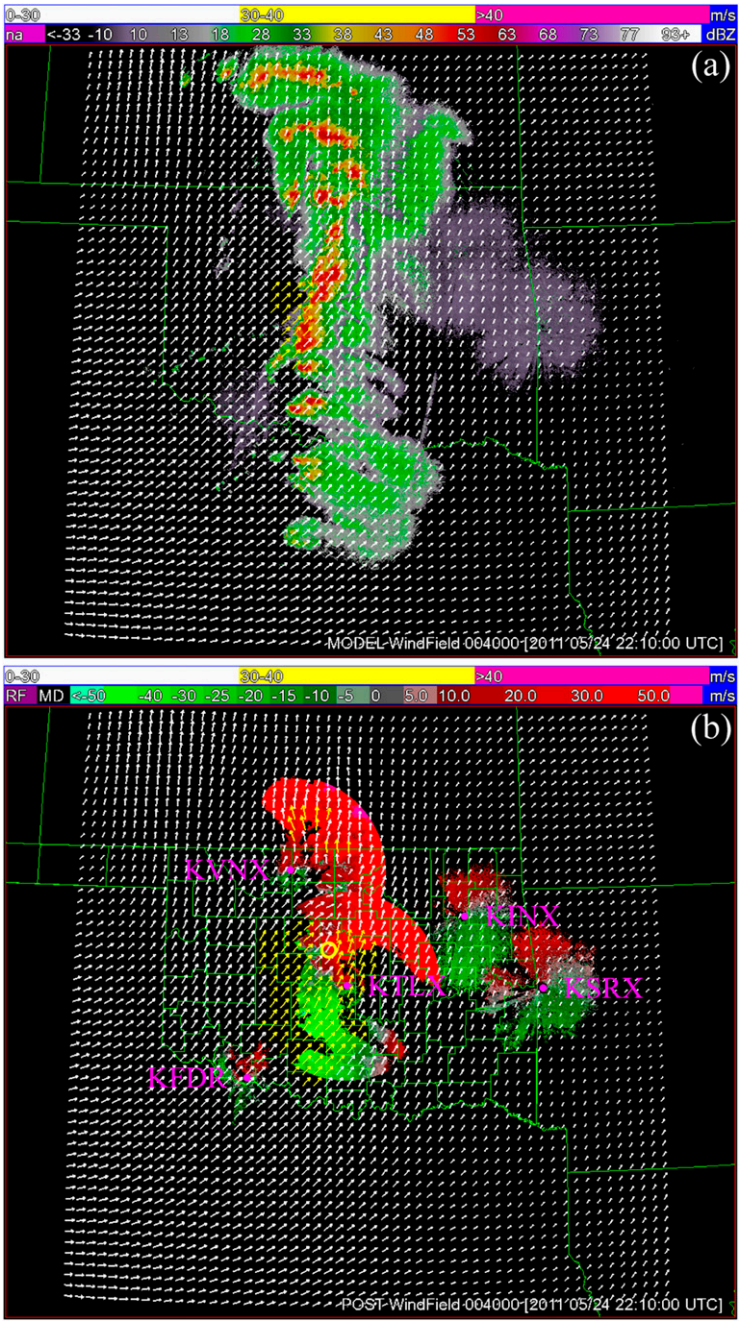

FIG. 1. (a) RAP forecast wind field plotted by color-scaled arrows on the 800 × 800 km^2 horizontal domain at $z = 4$ km superimposed on the reflectivity image from five radars for the tornadic storm at 2211 UTC 24 May 2011. (b) As in (a), but for the RWAS-analyzed wind field superimposed on the dealiased radial-velocity images at 4.0° tilt from KTLX and the Vance Air Force Base, Oklahoma (KVNX) radar; 0.9° tilt from KFDR; and 0.5° tilt from the Tulsa, Oklahoma (KINX), and the Fort Smith, Arkansas (KSRX) radars. In (b), the image from KTLX covers the image from KVNX, while the images from the remaining three radars are largely isolated around their respective radars. Positive (negative) values shown by the image from any one of the radars indicate horizontal flow away from (toward) that radar, while zero or near-zero values indicate flow perpendicular to the viewing direction from that radar. Each radar site is marked by a purple dot with the radar name in (b). The small yellow circle in (b) marks the tornadic mesocyclone. The thin green lines plot the state boundaries in (a) and (b), and the county boundaries in Oklahoma only in (b).

RWAS-produced incremental wind field is limited by the superobservation resolution and the decorrelation length of the background error correlation function used in the analysis. As shown in Fig. 1b, the mesocyclone is about 100 km away from KTLX, so the decorrelation length is 18 km and the superobservation resolution is coarsened to 21 km around the mesocyclone. The effective analysis resolution is thus limited by 21 km, which is obviously insufficient to resolve the mesocyclone. In addition, the ability of the existing RWAS to retrieve the unobserved wind component tangential to the radar beam is limited by the homogeneous and isotropic background error correlation functions [see (2) in Xu et al. (2015)] used for the vector wind analysis. This is the second limitation.

3. Vortex wind analysis

To resolve the mesocyclone, it is necessary to overcome the aforementioned two limitations. To this end, a new method is developed with the following three key components: 1) an algorithm for estimating the vortex center of the mesocyclone on a selected tilt of a radar radial-velocity scan, 2) a vortex-flow-dependent background error correlation function formulated for the vortex wind analysis over the mesocyclone area on the selected tilt, and 3) the square root of the vortex-flow-dependent background error covariance matrix derived analytically to precondition the cost function and thus enhance the computational efficiency. The method can be used as an additional (fourth) step of targeted finescale analysis after the third step is performed in the RWAS. It can be also used in a standalone fashion. In the latter case, it is necessary to estimate the environmental mean wind. The detailed techniques in the three components are presented in the following subsections.

a. Estimating vortex center location and environmental mean wind

The mesocyclone area is identified as a by-product of the automated velocity dealiasing [see the appendix in Xu et al. (2013)] on a selected tilt of low-elevation radar scan, and this is done by applying four cyclonic-rotation conditions to an 11 × 41 data window (11 beams and 41 range gates) centered at each flagged special data point that fails to pass a tightened continuity condition. The vortex center location is then estimated, also as a by-product of the automated velocity dealiasing, and is used here as the first guess. From this first guess, the vortex center location is further estimated in the mesocyclone area on the selected tilt by applying the following two-step algorithm to the data field of dealiased radial-velocity observations, denoted by $v_r^o(r, \varphi)$, where r is the radial distance from the radar, φ is the radar beam azimuthal angle (positive for clockwise rotation from the y coordinate pointing to the north) on the selected tilt, and superscript o indicates observed and dealiased.

1) Find $v_{r_{\rm mx}} \equiv \max\,[v_r^o(\varphi)] = v_r^o\,(\varphi_{\rm mx})$ and $v_{r_{\rm mn}} \equiv \min[v_r^o(\varphi)] = v_r^o(\varphi_{\rm mn})$ along each range circle of fixed r over the sector data area of 20-km arc length and 20-km radial range centered at the aforementioned first guess of the vortex center. Here, $\varphi_{\rm mx}$ (or $\varphi_{\rm mn}$) is the azimuthal angle of the data point at which $v_r^o(r, \varphi)$ reaches $v_{r_{\rm mx}}$ (or $v_{r_{\rm mn}}$), and φ increases (or decreases) for a clockwise (or counterclockwise) rotation within the sector data area. Denote by r_{c_0} the radial range at which $(v_{r_{\rm mx}} - v_{r_{\rm mn}})/(\varphi_{\rm mx} - \varphi_{\rm mn})$ is the largest with the following three empirical conditions satisfied:

$$\varphi_{\rm mx} > \varphi_{\rm mn}, \quad v_{r_{\rm mx}} - v_{r_{\rm mn}} > 30\,{\rm m\,s^{-1}}, \quad \text{and}$$
$$(v_{r_{\rm mx}} - v_{r_{\rm mn}})/\varphi_{\rm mx} - \varphi_{\rm mn} > 20\,{\rm m\,s^{-1}}(1^\circ)^{-1}. \quad (1)$$

Denote by φ_{c_0} the value of $(\varphi_{\rm mx} + \varphi_{\rm mn})/2$ on the range circle of $r = r_{c_0}$. The initial estimate of the vortex center location is given by (r_{c_0}, φ_{c_0}).

2) Denote by v_r^c the value of v_r^o interpolated at (r_{c_0}, φ_{c_0}). Find the location, denoted by $(r_j, \varphi_j) = (j\Delta r, \varphi_j)$, where $v_r^{oc}(r, \varphi) \equiv v_r^o(r, \varphi) - v_r^c$ changes sign from negative to positive as φ increases from $\varphi_{j-} \equiv \varphi_j - m\Delta\varphi/2$ to $\varphi_{j+} \equiv \varphi_j + m\Delta\varphi/2$ with $1 \le m \le 2$ along the jth range circle in the same sector data area as described in the previous step. Here, Δr (=250 m) is the radar range gate spacing, $\Delta\varphi$ (=1°) is the beam spacing in the azimuth, and m = 1 (or 2) means that there is no gap (or only one gap) between the two nonmissing azimuthal data points where the sign change of v_r^{oc} is detected. The increment of v_r^{oc} associated with the sign change of v_r^{oc} from point $(j\Delta r, \varphi_{j+})$ to point $(j\Delta r, \varphi_{j-})$ along the jth range circle is denoted and defined by $\Delta v_{r_j} \equiv v_r^{oc}(j\Delta r, \varphi_{j+}) - v_r^{oc}(j\Delta r, \varphi_{j-}) > 0$. The final estimate of the vortex center location is given by

$$(r_c, \varphi_c) = \sum_j (r_j, \varphi_j)(\Delta v_{r_j}/\Delta l_j)^2 \Big/ \sum (\Delta v_{r_j}/\Delta l_j)^2, \quad (2)$$

where $(\Delta l_j)^2 = (r_j - r_{c_0})^2 + r_j^2(\varphi_j - \varphi_{c_0})^2$ and the summation is over j for up to five range circles that have the first five largest values of Δv_{r_j}.

As by-products, the maximum tangential velocity for the vortex and its radial distance from the vortex center are estimated, respectively, by

$$V_M = (v_{r_{\rm max}} - v_{r_{\rm min}})/2 \quad (3)$$

and

$$R_M = (\Delta l_{\max} + \Delta l_{\min})/2, \tag{4}$$

where $v_{r_{\max}} \equiv \max[v_r^o(r, \varphi)] = v_r^o(r_{\max}, \varphi_{\max})$, $v_{r_{\min}} \equiv \min[v_r^o(r, \varphi)] = v_r^o(r_{\min}, \varphi_{\min})$, $(r_{\max}, \varphi_{\max})$ [or $(r_{\min}, \varphi_{\min})$] is the data point in the (r, φ) coordinates at which v_r^o reaches $v_{r_{\max}}$ (or $v_{r_{\min}}$) over the same sector data area as in the second step above, $(\Delta l_{\max})^2 = (r_{\max} - r_c)^2 + r_{\max}^2(\varphi_{\max} - \varphi_c)^2$, and $(\Delta l_{\min})^2 = (r_{\min} - r_c)^2 + r_{\min}^2(\varphi_{\min} - \varphi_c)^2$. Here, V_M and R_M are estimated by neglecting the divergent part of the vortex winds and assuming $R_M \ll r_c$. If the vortex center is very close to the radar and thus r_c becomes close to R_M, then (3) and (4) should be modified as shown in Wood and Brown (1992). This extreme situation, however, is not encountered and thus not considered in this paper. On the other hand, if the vortex is very far from the radar and the radar beam becomes wider than the vortex core diameter, then the sampled $v_{r_{\max}}$ at $\varphi_{\max}$ and $v_{r_{\min}}$ at $\varphi_{\min}$ will degrade too severely (in accuracy and resolution) to be used to reliably estimate V_M in (3) and R_M in (4). This extreme situation will be encountered in one of the cases presented in section 4.

After the vortex center location is estimated, the background wind field, denoted by (u^b, v^b), produced by the RWAS (see step 3 in section 2) is interpolated onto the radar radial-velocity observation points over a $20 \times 20\,\text{km}^2$ area centered at (r_c, φ_c) on the selected tilt. The radial component of the background wind is given by $v_r^b(r, \varphi) = (u^b \sin\varphi + v^b \cos\varphi)\cos\theta$ at each observation point (r, φ), where $\theta = \theta_e + \arctan[r\cos\theta_e/(4R_E/3 + r\sin\theta_e)]$ is the slope angle of the radar beam relative to the earth's surface beneath the observation point, θ_e is the beam elevation angle from the radar for the selected tilt, R_E is the earth's radius, and $4R_E/3$ is an "inflated" value of the earth's radius in the equivalent Earth model to consider the effects of atmospheric refraction [see (9.9) of Doviak and Zrnic (2006)]. The radial-velocity innovations, defined by

$$v_r^i(r, \varphi) \equiv v_r^o(r, \varphi) - v_r^b(r, \varphi) \text{ in the observation space}, \tag{5a}$$

are interpolated onto a 81×81 grid (with $\Delta x = \Delta y = 0.25\,\text{km}$) over the nested domain by

$$v_r^i(\mathbf{x}_i) = \sum_j v_r^i(\mathbf{x}_j) w_{ij} \Big/ \sum_j w_{ij}, \tag{5b}$$

where $\mathbf{x} \equiv (x, y)$, $v_r^i(\mathbf{x}_i)$ is the value of the radial-velocity innovation interpolated at $\mathbf{x}_i$, the summation is over j, $w_{ij} = \exp[-|\mathbf{x}_i - \mathbf{x}_j|^2/(2l_o^2)]$, $\mathbf{x}_i$ (or $\mathbf{x}_j$) denotes the ith grid point (or jth observation point) in the (x, y) coordinates over the nested domain, and $l_o = \max(r_c\Delta\varphi,\ 0.1\,\text{km})$. Here, l_o is bounded below by 0.1 km ($=0.4\Delta r$) for adequate filtering when $r_c\Delta\varphi < 0.1$ km.

If the environmental wind field around the vortex is well represented by the background wind field, then $v_{r_{\text{mx}}}^i$ and $v_{r_{\text{mn}}}^i$ should have about the same absolute value with opposite signs, where $v_{r_{\text{mx}}}^i$ and $v_{r_{\text{mn}}}^i$ are the maximum and minimum of interpolated $v_r^i(\mathbf{x}_i)$ in (5b), respectively, within the $2R_M$ radial range from the vortex center. In this case, $v_{r+} \equiv v_{r_{\text{mx}}}^i + v_{r_{\text{mn}}}^i$ should be much smaller than $v_{r-} \equiv v_{r_{\text{mx}}}^i - v_{r_{\text{mn}}}^i$ and thus should satisfy the following condition:

$$v_{r+} \ll v_{r-}. \tag{6}$$

If the condition in (6) is not well satisfied, then the environmental wind field around the vortex is not well captured by the background wind field and v_{r-} can represent the radial component of the averaged vector velocity difference, denoted by (u^e, v^e), between the environmental and background wind over the vortex area. In this case, (u^e, v^e) can be estimated by solving

$$\begin{aligned} v_{r+_A} &= u^e \sin\varphi_{c_A} + v^e \cos\varphi_{c_A} \quad \text{and} \\ v_{r+_B} &= u^e \sin\varphi_{c_B} + v^e \cos\varphi_{c_B}, \end{aligned} \tag{7}$$

which gives, for $\sin(\varphi_{c_A} - \varphi_{c_B}) \neq 0$,

$$\begin{aligned} u^e &= (v_{r+_A}\cos\varphi_{c_B} - v_{r+_B}\cos\varphi_{c_A})/\sin(\varphi_{c_A} - \varphi_{c_B}) \quad \text{and} \\ v^e &= (-v_{r+_A}\sin\varphi_{c_B} + v_{r+_B}\sin\varphi_{c_A})/\sin(\varphi_{c_A} - \varphi_{c_B}), \end{aligned} \tag{8}$$

where v_{r+_A} (or v_{r+_B}) is the value of v_{r+} computed from radar A (or B) and φ_{c_A} (or φ_{c_B}) is the value of φ_c estimated in (2) for radar A (or B). Here, as indicated by (7), v_{r+_A} (or v_{r+_B}) is taken to be the radial component of (u^e, v^e) with respect to radar A (or B).

If $\sin(\varphi_{c_A} - \varphi_{c_B}) = 0$ or v_{r+} is from a single radar, then the two equations in (7) reduce to a single equation and (u^e, v^e) cannot be estimated by (8). In this case, (u^e, v^e) can be only unreliably estimated by neglecting its component perpendicular to the radar beam and this gives

$$(u^e, v^e) = v_{r+}(\sin\varphi_c, \cos\varphi_c). \tag{9}$$

If the environment winds are strong [and thus do not satisfy (6)] and mostly perpendicular to the radar beams around the mesocyclone, then the environmental mean wind cannot be correctly estimated by (9). In this case, as will be shown in section 4b, by assuming that the vortex center moves mainly with the environment wind, the vortex center moving velocity, denoted by (u^c, v^c) and estimated by the time change rate of the vortex center location (on the same tilt from the previous to the

current volume scan), can be used as the environmental mean wind, instead of (u^e, v^e) in (9), for the stand-alone single-Doppler vortex wind analysis.

After (u^e, v^e) is estimated, v_r^i is adjusted at each observation point to

$$v_r^{ie}(r,\varphi) \equiv v_r^i(r,\varphi) - v_r^e(r,\varphi), \tag{10}$$

where $v_r^e(r,\varphi) = (u^e \sin\varphi + v^e \cos\varphi)\cos\theta$ is the radial component of (u^e, v^e) computed at observation point (r, φ). Here, v_r^{ie} is defined as an adjusted radial-velocity innovation with respect to the adjusted background radial-velocity $v_r^b(r,\varphi) + v_r^e(r,\varphi)$.

If the vortex wind analysis is performed in a stand-alone fashion with zero (u^b, v^b), then v_r^i reduces to v_r^o in (5a). In this case, (6) is often not satisfied, and it is necessary to estimate (u^e, v^e) and use it as a proxy background wind. The estimation can be done as described above by using (8) or (9) except that v_r^i reduces to v_r^o in (5).

b. Cost function formulated with vortex-flow-dependent background error covariance

The control variables used for the vortex wind analysis are the radial velocity V_R (>0 in the outward direction), and the tangential velocity V_T (>0 in the counterclockwise direction), of the vortex part of the mesocyclone wind field. This vortex part is an incremental wind field, denoted by $(\Delta u, \Delta v)$, with respect to the background wind field (u^b, v^b) [or adjusted background wind field $(u^b, v^b) + (u^e, v^e)$] if the innovation data v_r^i [or adjusted innovation data v_r^{ie} in (10)] are used by the analysis. In the local (x, y)-coordinate system centered at (r_c, φ_c) on the selected tilt, the horizontal vector velocity increment $(\Delta u, \Delta v)$ is related to (V_R, V_T) by

$$(\Delta u, \Delta v) = (V_R \cos\beta - V_T \sin\beta,\ V_R \sin\beta + V_T \cos\beta), \tag{11}$$

where $\beta \equiv \arctan(y/x)$. The radar-observed radial component of $(\Delta u, \Delta v)$ can be modeled by

$$\begin{aligned} v_r &= (\Delta u \sin\varphi + \Delta v \cos\varphi)\cos\theta \\ &= [(V_R\cos\beta - V_T\sin\beta)\sin\varphi + (V_R\sin\beta + V_T\cos\beta)\cos\varphi]\cos\theta \\ &= [V_R \sin(\varphi+\beta) + V_T\cos(\varphi+\beta)]\cos\theta, \end{aligned} \tag{12}$$

where the projection of the vertical velocity w is neglected in (12) since θ is small (<5°) and w is not analyzed.

The cost function for the vortex wind analysis has the following form:

$$J = \mathbf{a}^{\mathrm{T}}\mathbf{B}^{-1}\mathbf{a}/2 + (\mathbf{Ha} - \mathbf{d})^{\mathrm{T}}\mathbf{O}^{-1}(\mathbf{Ha} - \mathbf{d})/2, \tag{13}$$

where $\mathbf{a} \equiv (\mathbf{a}_R^{\mathrm{T}}, \mathbf{a}_T^{\mathrm{T}})^{\mathrm{T}}$, $\mathbf{a}_R$ (or $\mathbf{a}_T$) is the state vector of V_R (or V_T), $(\cdot)^{\mathrm{T}}$ denotes the transpose of $(\cdot)$, $\mathbf{B}$ is the background error covariance matrix, $\mathbf{O}$ is the observation error covariance matrix, $\mathbf{H}$ is the observation operator expressed in (12) (for observations from any given radars), and $\mathbf{d}$ is the innovation (or adjusted innovation) vector, that is, the state vector of v_r^i (or v_r^{ie}) [see (10)]. The observation errors are assumed to be uncorrelated between different points, so $\mathbf{O} = \sigma_o^2\mathbf{I}$ where σ_o^2 is the observation error variance and $\mathbf{I}$ is the unit matrix in the observation space.

The random vector fields of background wind errors, denoted by $(\boldsymbol{\varepsilon}_R, \boldsymbol{\varepsilon}_T)$, are assumed to have zero mean; that is, $\langle\boldsymbol{\varepsilon}_T\rangle = \langle\boldsymbol{\varepsilon}_R\rangle = 0$, where $\langle(\cdot)\rangle$ denotes the statistical mean of $(\cdot)$. In addition, it is also assumed that $\boldsymbol{\varepsilon}_R$ and $\boldsymbol{\varepsilon}_T$ are not correlated and are nearly homogeneous and isotropic in the following transformed polar coordinates:

$$\rho \equiv l^{-1}\ln(1 + R/R_c) \quad \text{and} \tag{14a}$$

$$\phi \equiv \beta/\Phi, \tag{14b}$$

where $R = |\mathbf{x}| = (x^2 + y^2)^{1/2}$; l and Φ are the scaling factors for ρ and ϕ, respectively; and R_c is the scaling factor for R and is set to $R_c = 1$ km according the averaged horizontal resolution of radar radial-velocity observations.

The above-assumed near homogeneity and isotropy imply that the covariance tensor function for $\boldsymbol{\varepsilon} = (\boldsymbol{\varepsilon}_R, \boldsymbol{\varepsilon}_T)^{\mathrm{T}}$ has the following diagonal form:

$$\mathbf{B} \equiv \langle\boldsymbol{\varepsilon}_i\boldsymbol{\varepsilon}_j^{\mathrm{T}}\rangle = (B_R, B_T)^{\mathrm{diag}}. \tag{15a}$$

The two diagonal components of $\mathbf{B}$ are modeled by

$$\begin{aligned} B_R &= \sigma_R^2 C(\rho_i, \rho_j; \phi_i - \phi_j) \quad \text{and} \\ B_T &= \sigma_T^2 C(\rho_i, \rho_j; \phi_i - \phi_j), \end{aligned} \tag{15b}$$

where σ_R (or σ_T) is the standard deviation of $\boldsymbol{\varepsilon}_R$ (or $\boldsymbol{\varepsilon}_T$) and $C(\rho_i, \rho_j; \phi_i - \phi_j)$ is a pseudocorrelation function constructed by

$$C(\rho_i, \rho_j; \phi_i - \phi_j) = C_1(\rho_i, \rho_j)C_2(\phi_i - \phi_j), \tag{16a}$$

$$\begin{aligned} C_1(\rho_i, \rho_j) = \exp[-(\rho_i - \rho_j)^2/2] \\ - \exp[-(\rho_i + \rho_j)^2/2], \quad \text{and} \end{aligned} \tag{16b}$$

$$C_2(\phi_i-\phi_j)=A_0^{-1}\sum_n \exp[-(\phi_i-\phi_j-2n\pi/\Phi)^2/2]$$
$$\approx \exp[-(\phi_i-\phi_j)^2/2] \quad \text{for} \quad -\pi/\Phi\le\phi_i-\phi_j\le\pi/\Phi \quad \text{and} \quad \Phi\le 1, \tag{16c}$$

where $A_0=\sum_n \exp[-2(n\pi)^2/\Phi^2]>1$ to ensure $C_2(0)=1$ and $\sum_n$ denotes the summation over integer n from $-\infty$ to ∞. For $\Phi\le 1$, $A_0\approx 1$ and the summation in (16c) can be truncated to a single term as shown in the last step of (16c).

In (16b), the Gaussian correlation function is modified by subtracting its mirror image obtained by mirror reflecting the corrected point ρ_i (or ρ_j) with respect to $\rho=0$, so $C_1(\rho_i,\rho_j)$ can have the desired property of $C_1(\rho_i,\rho_j)=0$ for $\rho_i=0$ or $\rho_j=0$ to ensure the analyzed V_R and V_T always approach to zero toward the vortex center. In (16c), the Gaussian correlation function is extended periodically over the periodic domain of $-\pi/\Phi<\phi\le\pi/\Phi$ in (16c) similarly to that in (1b) of Xu and Wei (2011). In this paper, only the reduced form of $C_2(\phi_i-\phi_j)$ in the last step of (16c) will be used with $\Phi=1$. Figures 2a and 2b show the structures of $C(\rho_i,\rho_j;\phi_i-\phi_j)$ around two points (labeled A and B) in the transformed (ρ,ϕ) and original (x,y) coordinates, respectively, where $l=1/2$ and $\Phi=1$. From (16) and Fig. 2a, we can see that $C(\rho_i,\rho_j;\phi_i-\phi_j)$ is nearly homogeneous and isotropic when $\rho_i>1$ and $\rho_j>1$, and becomes virtually homogeneous and isotropic when $\rho_i>2$ and $\rho_j>2$ in the transformed (ρ,ϕ) space but is stretched in the azimuthal direction along the curved vortex flow in the original (x,y) space.

Since the radial decorrelation length equals 1 in ρ, the associated radial decorrelation length in the physical space can be estimated by $R_c\exp[l(\rho+1/2)]-R_c\exp[l(\rho-1/2)]=2R\sinh(l/2)$. The radial decorrelation length in the physical space is thus a linear function of R, which is similar to the azimuthal decorrelation arc length, that is, ΦR as a linear function of R. With this property, the correlation structure defined by $C(\rho_i,\rho_j;\phi_i-\phi_j)$ as a function of $\mathbf{x}_j$ for a given $\mathbf{x}_i$ is nearly invariant in shape but its size increases linearly with $|\mathbf{x}_i|$. When $|\mathbf{x}_i|$ reaches the boundaries of the nested domain (of $2L\times 2L$ with $L=10$ km), the radial decorrelation length in the physical space increases to $2L\sinh(l/2)\approx 6$ km (for $l=1/2$) and the azimuthal decorrelation arc length increases to $\Phi L=10$ km (for $\Phi=1$). These increased decorrelation lengths around the nested domain boundaries are compatible with the decorrelation length (=11 km) used by the RWAS in the last step to produce the mesoscale background wind field (see step 3 in section 2) for the vector wind analysis.

As shown above, l and Φ control the decorrelation lengths in the physical space along the radial and azimuthal directions, respectively. These scaling factors are specified empirically in this paper. The background wind error correlation structures and associated decorrelation lengths in the radial and azimuthal directions may be estimated statistically from time series of radar radial-velocity observations of mesocyclones by modifying the innovation method of Xu et al. (2007) with the covariance model used in this paper. This approach needs to be explored beyond this paper.

c. *Square root of background error covariance and preconditioned cost function*

The square root of the background error covariance matrix can be derived analytically as shown below. First, one can verify that the correlation functions defined in (16b) and (16c) can be expressed by the following integrals:

$$C_1(\rho_i,\rho_j)=\int_0^\infty P_1(\rho_i,\rho_s)P_1(\rho_s,\rho_j)\,d\rho_s \quad \text{and} \tag{17a}$$
$$C_2(\phi_i-\phi_j)=\int_{-\pi}^{\pi} P_2(\phi_i-\phi_s)P_2(\phi_s-\phi_j)\,d\phi_s, \tag{17b}$$

where

$$P_1(\rho_i,\rho_s)\equiv(2/\pi)^{1/4}\{\exp[-(\rho_i-\rho_s)^2]-\exp[-(\rho_i+\rho_s)^2]\} \quad \text{and} \tag{18a}$$
$$P_2(\phi)\equiv(2/\pi)^{1/4}A_0^{-1/2}\sum_n \exp[-(\phi-2n\pi/\Phi)^2]$$
$$\approx(2/\pi)^{1/4}\exp(-\phi^2) \quad \text{for} \quad -\pi/\Phi\le\phi\le\pi/\Phi \quad \text{and} \quad \Phi\le 1. \tag{18b}$$

The truncation error for the approximation in the last step of (18b) is within $\pm\exp(-\pi^2/\Phi^2)$, and $\exp(-\pi^2/\Phi^2)\ll 1$ for $\Phi=1$.

For the wind analyses performed in this paper, the two correlated points $\mathbf{x}_i$ and $\mathbf{x}_j$ are confined within the range circle of $R=\sqrt{2}L$ that encircles the nested analysis domain, so ρ_i and ρ_j are confined between 0 and $\rho_{\max}\equiv l^{-1}\ln(1+\sqrt{2}L/R_c)=5.435$ (for $L=10$ km). Note that the integrand $P_1(\rho_i,\rho_s)P_1(\rho_s,\rho_j)$ in (17a) becomes negligibly small as $\rho_s>\rho_{\max}+2$ for ρ_i and ρ_j confined between 0 and $\rho_{\max}$. This implies that the integration

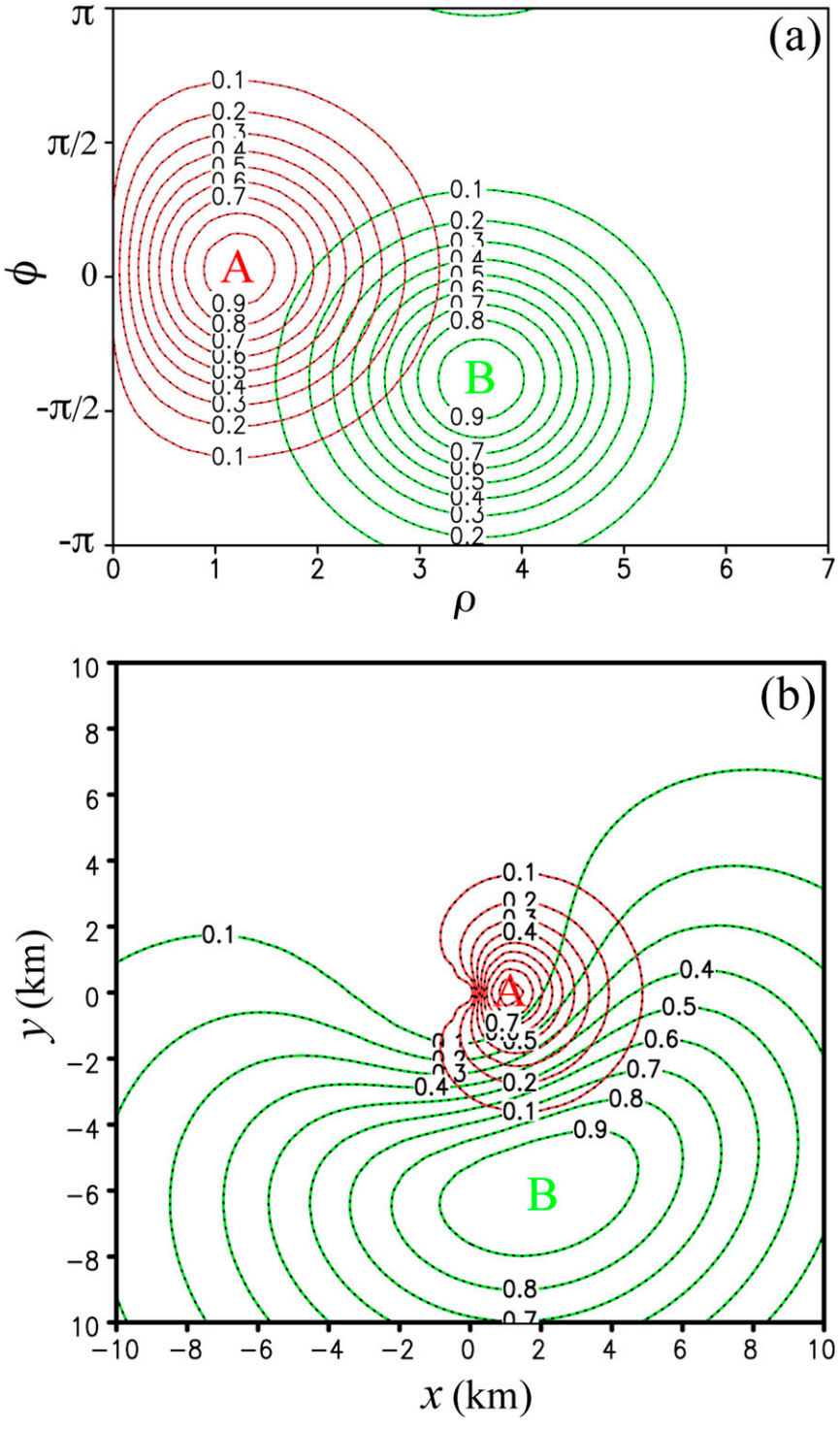

FIG. 2. (a) Plot of $C(\rho_i, \rho_j; \phi_i - \phi_j)$ in the transformed space by red and green contours as functions of (ρ_i, ϕ_i) for two fixed points of $(\rho_i, \phi_i) = (1.4, 0)$ and $(4.0, -0.4\pi)$ labeled by A and B, respectively. (b) Plot of $C(\mathbf{x}_i, \mathbf{x}_j)$ in the physical space by red and green contours as functions of $\mathbf{x}_i$ for the same two points of $\mathbf{x}_j = (1, 0)$ and $(2, -6)$ km labeled by A and B, respectively. Here, $R_c = 1$ km, $l = 1/2$, and $\Phi = 1$ for the coordinate transformation in (14). The black dotted contours that overlap the red (or green) contours plot the same correlation function as shown by the red (or green) contours but constructed from the square root matrix $\mathbf{P}$ by using (21).

range in (17a) can be reduced from $0 \le \rho_s < \infty$ to $0 \le \rho_s \le \rho_{\max} + 2$, so the integral in (17a) can be discretized into the following form:

$$C_1(\rho_i, \rho_j) \approx \sum_{s'} P_1(\rho_i, \rho_{s'}) P_1(\rho_{s'}, \rho_j) \Delta\rho = \sum_{s'} P_{1is'} P_{1s'j}, \tag{19}$$

where $P_{1is'} \equiv P(\rho_i, \rho_{s'})(\Delta\rho)^{1/2}$, $P_{1s'j} \equiv P(\rho_{s'}, \rho_j)(\Delta\rho)^{1/2}$, $\Delta\rho$ is the grad spacing of discretized $\rho_{s'} = (s' + 1/2)\Delta\rho$, the summation is over integer s' from 0 to $S \equiv \text{Int}[(\rho_{\max} + 2)/\Delta\rho]$, and Int[(·)] denotes the nearest integer of (·). To adequately resolve $P_1(\rho_i, \rho_{s'})$, $\Delta\rho$ should not exceed ½.

Similarly, the convolution integral in (17b) can be discretized into the following form:

$$C_2(\phi_i - \phi_j) \approx \sum_{s''} P_{2is''} P_{2s''j}, \tag{20}$$

where $P_{2is''} \equiv P_2(\phi_i - s''\Delta\phi)(\Delta\phi)^{1/2}$, $P_{2s''j} \equiv P_2(s''\Delta\phi - \phi_j)(\Delta\phi)^{1/2}$, $\Delta\phi = \pi/(M\Phi)$ is the grad spacing for discretized $\phi_{s''} = s''\Delta\phi$, and the summation is over integer s'' from $1 - M$ to M. To adequately resolve $P_2(\phi)$, $\Delta\phi$ should not exceed ½, so M must be larger than π/Φ. The truncated form of $P_2(\phi)$ at the last step of (18b) is used to compute $P_{2is''}$ and $P_{2s''j}$ for $\Phi = 1$.

Substituting (19) and (20) into (16a) gives

$$C(\rho_i, \rho_j; \phi_i - \phi_j) \approx \sum_{s'} \sum_{s''} P_{1is'} P_{1s'j} P_{2is''} P_{2is''j} = \sum_{s} P_{is} P_{sj}, \tag{21a}$$

where $P_{is} \equiv P_{1is'} P_{2is''}$ and the index s counts through all the grid points of (s', s'') over the two-dimensional control-variable domain with $0 \le s' \le S$ and $1 - M \le s'' \le M$. The matrix form of (21a) is

$$\mathbf{C} = \mathbf{P}\mathbf{P}^{\mathrm{T}}, \tag{21b}$$

where the ijth element of $\mathbf{C}$ is given by $C_1(\rho_i - \rho_j)C_2(\phi_i - \phi_j)$ with the index i (or j) counting through all the grid points over the two-dimensional analysis domain except for the central grid point (at the vortex center where Δu and Δv must be zero) and the isth element of $\mathbf{P}$ is given by $P_{is} = P_{1is}P_{2is} = P_1(\rho_i, \rho_s)P_2(\phi_i - \phi_s)(\Delta\rho\Delta\phi)^{1/2}$ with the index s counting through all the grid points of (s', s''). As shown in (21b), $\mathbf{P}$ is an analytically constructed square root of $\mathbf{C}$.

For the selected values of $l = ½$, $\Phi = 1$, and $R_c = 1$ km, the dimension of (s', s'') depends on $(\Delta\rho, \Delta\phi)$—the grid resolutions of the control-variable domain. Clearly, choosing relatively large $(\Delta\rho, \Delta\phi)$ can reduce the dimension of (s', s'') and, thus, improve the computational efficiency. On the other hand, $\Delta\rho$ and $\Delta\phi$ should not exceed ½ in order to adequately resolve $P_1(\rho)$ and $P_2(\phi)$. As an optimal trade-off, we set $\Delta\rho = ½$ and $\Delta\phi = \pi/(9\Phi)$ (<½). This gives $S = 15$ and $M = 9$, so the dimension of (s', s'') is $16 \times 18 = 288$, and the dimension of matrix $\mathbf{P}$ indexed by (s, i) is $288 \times [(2L/\Delta x + 1)^2 - 1]$, where Δx is the grid spacing for the analyzed fields in the nested domain excluding the grid point at the vortex center. With the above discretization, the correlation function constructed from the square root matrix $\mathbf{P}$ by using (21) is almost identical to the original correlation function formulated in (16), and the maximum difference is well within 1% for the examples shown in Fig. 2.

Substituting (21) into (15b) gives $\mathbf{B} = (\sigma_R^2\mathbf{C}, \sigma_T^2\mathbf{C})^{\text{diag}} = (\sigma_R\mathbf{P}, \sigma_T\mathbf{P})^{\text{diag}}(\sigma_R\mathbf{P}^{\mathrm{T}}, \sigma_T\mathbf{P}^{\mathrm{T}})^{\text{diag}}$, so $\mathbf{B}^{1/2} \equiv (\sigma_R\mathbf{P}, \sigma_T\mathbf{P})^{\text{diag}}$ is a square root of $\mathbf{B}$ satisfying $\mathbf{B}^{1/2}\mathbf{B}^{\mathrm{T}/2} = \mathbf{B}$. Substituting $\mathbf{a} = \mathbf{B}^{1/2}\mathbf{c}$ with $\mathbf{O} = \sigma_o^2\mathbf{I}$ into (13) gives

$$J = |\mathbf{c}|^2/2 + |\mathbf{H}'\mathbf{c} - \mathbf{d}/\sigma_o|^2/2, \tag{22}$$

where $\mathbf{H}' = \sigma_o^{-1}\mathbf{H}\mathbf{B}^{1/2}$ is the σ_o-scaled radial-velocity observation operator for the transformed control vector $\mathbf{c} \equiv (\mathbf{c}_R^{\mathrm{T}}, \mathbf{c}_T^{\mathrm{T}})^{\mathrm{T}}$, and the two components of the partitioned state vector $\mathbf{a} \equiv (\mathbf{a}_R^{\mathrm{T}}, \mathbf{a}_T^{\mathrm{T}})^{\mathrm{T}}$ are related to $\mathbf{c}_R$ and $\mathbf{c}_T$ by

$$\mathbf{a}_R = \sigma_R\mathbf{P}\mathbf{c}_R \quad \text{and} \tag{23a}$$

$$\mathbf{a}_T = \sigma_T\mathbf{P}\mathbf{c}_T. \tag{23b}$$

Substituting (23) into (11) gives

$$\Delta u(\mathbf{x}_i) = \sigma_R \cos\beta_i \sum_s P_{is}\mathbf{c}_{Rs} - \sigma_T \sin\beta_i \sum_s P_{is}\mathbf{c}_{Ts} \quad \text{and} \tag{24a}$$

$$\Delta v(\mathbf{x}_i) = \sigma_R \sin\beta_i \sum_s P_{is}\mathbf{c}_{Rs} + \sigma_T \cos\beta_i \sum_s P_{is}\mathbf{c}_{Ts}, \tag{24b}$$

where $\mathbf{x}_i$ denotes the ith grid point in the nested domain.

Substituting (24) into (12) gives

$$v_r(\mathbf{x}_i) = \cos\theta_i \left[\sigma_R \sin(\varphi_i + \beta_i) \sum_s P_{is}\mathbf{c}_{Rs} + \sigma_T \cos(\varphi_i + \beta_i) \sum_s P_{is}\mathbf{c}_{Ts}\right] = \sigma_R \sum_s R_{is}\mathbf{c}_{Rs} + \sigma_R \sum_s R_{is}\mathbf{c}_{Ts},$$

where $\mathbf{x}_i$ denotes the ith observation point over the nested domain, $R_{is} = \cos\theta_i \sin(\varphi_i + \beta_i)P_{is}$, and $T_{is} = \cos\theta_i \cos(\varphi_i + \beta_i)P_{is}$. Here, $\mathbf{H}' = \sigma_o^{-1}\mathbf{H}\mathbf{B}^{1/2}$ is derived analytically in the form of $\mathbf{H}' = (\sigma_R\mathbf{R}, \sigma_T\mathbf{T})/\sigma_o$ with the isth element of $\mathbf{R}$ (or $\mathbf{T}$) given by R_{is} (or T_{is}). Note that $\mathbf{x}_i$ can be any point in the continuous space of x excluding the vortex center, so the analytical form of $\mathbf{H}'$ can be applied to continuous observations

TABLE 1. Comparisons between the single- and dual-Doppler vortex wind analyses that use the RWAS-produced background wind field for the Oklahoma tornadic storm at 2211 UTC 24 May 2011. Here, V_M (or R_M) is the max tangential velocity of the vortex (or the radial distance of the max tangential velocity from the vortex center) estimated by (3) or (4) from single-Doppler radial-velocity observations, $V_{\max}$ (or $R_{\max}$) is the max tangential velocity (or the radial distance of the max tangential velocity from the vortex center) in the analyzed vortex wind field, and RMSd (or RMSd5) is the RMS deviation of the single-Doppler-analyzed vortex winds from the dual-Doppler-analyzed vortex winds over the nested domain (or within $R \le 5$ km from the vortex center).

Radar	V_M (m s^{-1})	R_M (km)	$V_{\max}$ (m s^{-1})	$R_{\max}$ (km)	RMSd (m s^{-1})	RMSd5 (m s^{-1})
KFDR	32.6	3.55	38.7	1.06	7.1	7.4
KTLX	32.8	2.23	34.1	0.56	8.6	8.6
KTLX and KFDR	—	—	38.8	0.56	—	—

to construct a more accurate integral-form observation operator [see (4.4) of Xu and Wei (2013)].

Since the nested domain is small, $\mathbf{c}_T$ and $\mathbf{c}_R$ are constructed on a 16×18 uniform (ρ, ϕ) grid with $\Delta\rho = \frac{1}{2}$ to cover the range of $0 \le \rho \le \rho_{\max} + 2$ and $\Delta\phi = \pi/(9\Phi)$ ($<\frac{1}{2}$) to cover the entire range of $-\pi/\Phi < \phi \le \pi/\Phi$. In this case, although the observation space dimension can exceed 10^4, the control-vector space dimension is merely $2 \times 16 \times 18 = 576$, so the preconditioned cost function in (22) can be minimized efficiently by using the conjugate-gradient descent algorithm. Substituting the minimizer $\mathbf{c}$ back into (24) gives the analyzed vortex wind field $(\Delta V_R, \Delta V_T)$. In particular, the vortex analysis takes less than 6 s of central processing unit (CPU) time for each case presented in section 4, while the three steps of RWAS wind analysis take about 3 min of CPU time on a workstation.

For the illustrative examples presented in the next section, the error standard deviation for the dealiased radial-velocity observations is set to $\sigma_o = 2\,\text{m s}^{-1}$ in the cost function, and this setting is the same as that used to estimate the superobservation error standard deviation [see section 3.3 of Xu et al. (2015)] for the vector wind analysis in step 3 of section 2. As we have seen in Fig. 1b, the RWAS-produced background winds are too smooth to capture the mesocyclone, so the background wind errors can be as large as the true vortex winds. Since the maximum of the true vortex winds estimated from $v_r^o(r, \varphi)$ by V_M in (3) ranges from 32 to 45 m s^{-1} (see Tables 1 and 4; Table 4 is described in greater detail below), $\sigma_T = \sigma_R = 20\,\text{m s}^{-1}$ can be used for constructing the preconditioned cost function in (22).

4. Illustrative examples

a. *Vortex wind analyses performed with RWAS*

The vortex wind field for the tornadic mesocyclone (marked by the small yellow circle in Fig. 1b) on 24 May 2011 is analyzed in this section as an incremental wind field with respect to the RWAS-produced background wind field. The analyses are performed by using single-Doppler wind observations (dealiased v_r^o) from the WSR-88D in Fredrick, Oklahoma (KFDR), first and then KTLX. After this, the dual-Doppler wind analysis is performed by using observations from the two radars. Each single-Doppler-analyzed wind field estimates the horizontal winds on the radar-scanned slant surface, while the dual-Doppler-analyzed wind field estimates the horizontal winds averaged over the time interval between the two radar scans and in the vertical layer between the two radar-scanned slant surfaces. The vortex wind field analyzed from the KFDR radial-velocity innovation data on the 0.5° tilt (around $z = 4.29$ km) at 2210:15 UTC is plotted in Fig. 3a by the black arrows superimposed on the color contours of the KFDR radial-velocity innovation field [computed by (5b) on an 81×81 grid with $\Delta x = \Delta y = 0.25$ km] in the nested domain. The estimated vortex center is at $(r_c, \varphi_c) = (201.125\,\text{km}, 38.2°)$ in the KFDR coordinates. As shown in Fig. 3a, this estimated vortex center is not exactly on the solid green zero-v_r^i contour (as it should be) and is off the zero-v_r^i contour by about $0.3\Delta\varphi = 0.3°$ or $0.3r_c\Delta\varphi \approx 1$ km in the azimuthal direction with respect to KFDR, so the analyzed vortex wind field does not closely match the KFDR radial-velocity innovation field within the 1-km radial range around the vortex center. Outside the 1-km radial range, the analyzed vortex wind field matches the KFDR radial-velocity innovation field. The vortex wind field analyzed from the KTLX radial-velocity innovation data on the 4.0° tilt (around $z = 4.44$ km) at 2212:23 UTC is plotted in Fig. 3b. The estimated vortex center is at $(r_c, \varphi_c) = (60.125\,\text{km}, 332°)$ in the KTLX coordinates. This estimated vortex center is very close to the solid green zero-v_r^i contour, and the analyzed vortex wind field matches the KTLX radial-velocity innovation field very well.

For the vortex winds in Fig. 3a (or Fig. 3b), the maximum velocity is $V_{\max} \equiv \max|(\Delta u, \Delta v)| = 38.7$ (or 34.1) m s^{-1} at the radial distance of $R_{\max} = 1.06$ (or 0.56) km from the vortex center, as listed in the first (or second) row of Table 1. For KFDR, the listed value of $V_{\max} = 38.7\,\text{m s}^{-1}$ is slightly larger than the maximum tangential velocity $V_M = 32.6\,\text{m s}^{-1}$ estimated by (3), but the listed value of $R_{\max} = 1.06$ km is much smaller than

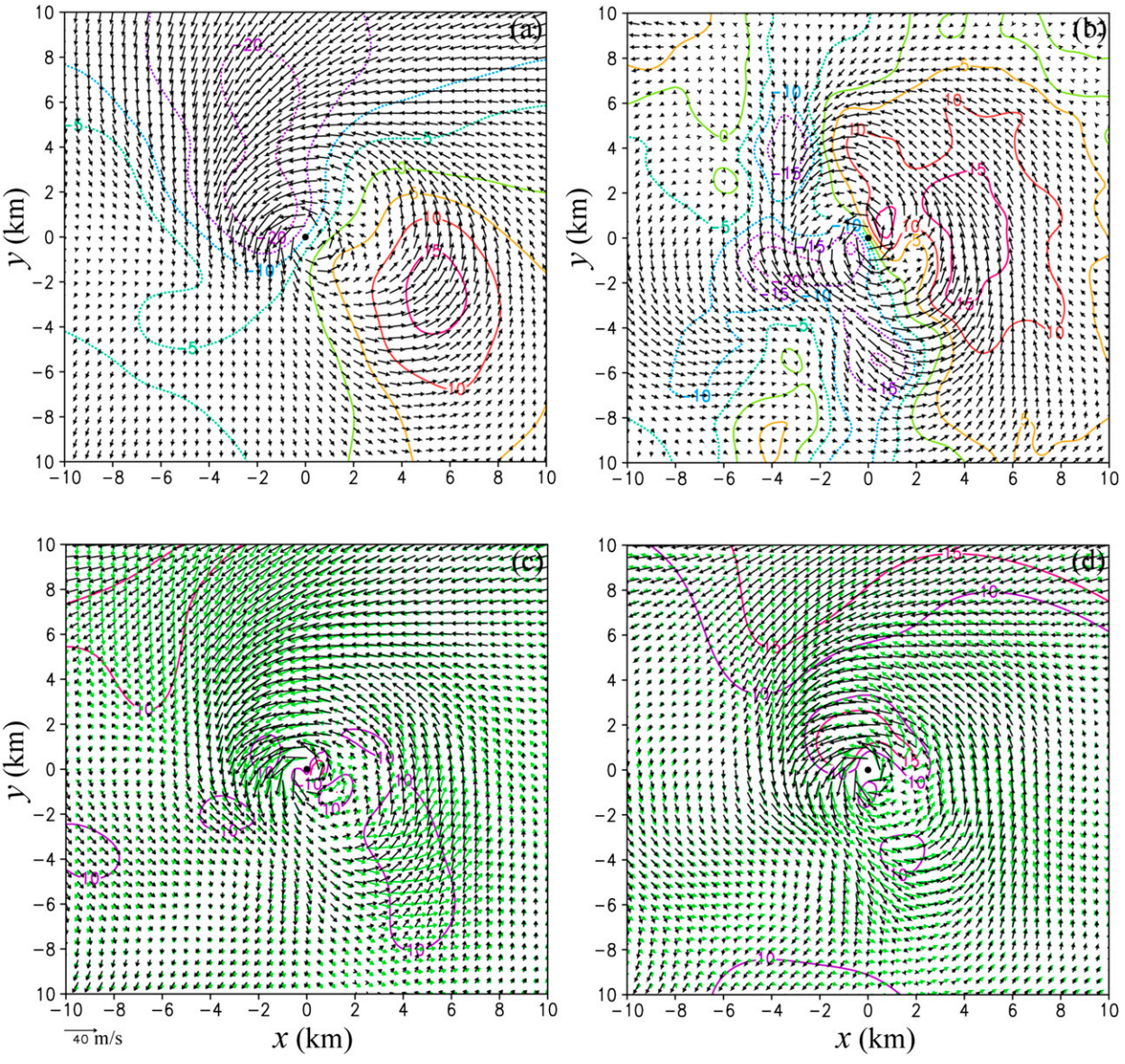

FIG. 3. (a) Single-Doppler-analyzed vortex winds plotted by black arrows superimposed on color contours of the radial-velocity innovation field v_r^i at 0.5° tilt ($z \approx 4.28$ km) from KFDR at 2210:15 UTC 24 May 2011. (b) As in (a), but for 4.0° tilt ($z \approx 4.42$ km) from KTLX at 2212:23 UTC 24 May 2011. (c) Dual-Doppler-analyzed vortex winds plotted by black arrows together with the single-Doppler-analyzed vortex winds from KFDR as in (a) but replotted by green arrows and superimposed on color contours of absolute value of the vector difference between the single- and dual-Doppler-analyzed vortex winds. (d) As in (c), but for the single-Doppler-analyzed vortex winds from KTLX as in (b). The analysis domain is centered at the estimated vortex center (plotted by the black heavy dot), while KFDR and KTLX are located at $(x, y) = (-124.28, -158.06)$ and $(28.23, -53.09)$ km outside the analysis domain, respectively.

the $R_M = 3.55$ km estimated by (4) because R_M is bounded below by the azimuthal resolution ($r_c\Delta\varphi \approx 3.5$ km) of the KFDR observations around the vortex center. Clearly, with $r_c = 201.125$ km, the vortex is too far from KFDR, so V_M and R_M cannot be reliably estimated by (3) and (4) from the KFDR observations, as explained in section 3a. For KTLX, the listed value of $V_{\max} = 34.1\,\mathrm{m\,s^{-1}}$ is close to the maximum tangential velocity $V_M = 32.8\,\mathrm{m\,s^{-1}}$ estimated by (3), but the listed value of $R_{\max} = 0.56$ km is again much smaller than the $R_M = 2.23$ km estimated by (4) although R_M is not close to the low bound of $r_c\Delta\varphi \approx 1$ km.

The radial-velocity innovation fields in Figs. 3a and 3b are separated in time (or height) by merely about 2 min (or 0.15 km), so these two data fields can be used together to analyze the averaged vortex wind field over

TABLE 2. As in the last four columns of Table 1, but for vortex wind analyses using the adjusted radial-velocity innovation data [see (10)]. In the first column, (u^e, v^e) is estimated by (9) for each single-Doppler vortex wind analysis and by (8) for the dual-Doppler vortex wind analysis.

Radar	(u^e, v^e) (m s^{-1})	V_{max} (m s^{-1})	R_{max} (km)	RMSd (m s^{-1})	RMSd5 (m s^{-1})
KFDR	(−2.3, −2.9)	35.0	0.90	7.7	8.0
KTLX	(1.3, −2.5)	32.9	0.56	7.1	6.6
KTLX and KFDR	(−1.1, −3.8)	35.3	0.71	—	—

the time interval between 2210:15 and 2212:23 UTC and in the vertical layer between $4.29 \le z \le 4.44$ km. The dual-Doppler-analyzed vortex wind field is plotted by the black arrows in Fig. 3c (or Fig. 3d) against the green arrows that replot the single-Doppler-analyzed vortex wind field in Fig. 3a (or Fig. 3b). As shown in Fig. 3c (or Fig. 3d), the KFDR (or KTLX) single-Doppler-analyzed vortex winds match the dual-Doppler-analyzed vortex winds with the absolute value of their vector difference below 10 m s^{-1} in most areas (outside the purple contour loops). As listed in the last two columns of Table 1, the root-mean-square (RMS) deviation of the KFDR (or KTLX) single-Doppler-analyzed vortex winds from the dual-Doppler-analyzed vortex winds is RMSd = 7.1 (or 8.6) m s^{-1} over the nested domain and is RMSd5 = 7.4 (or 8.6) m s^{-1} within $R \le 5$ km from the vortex center. These RMSd and RMSd5 values are much smaller (by about 5 times) than the V_{max} listed in the third column of Table 1.

The radial-velocity innovation field in Fig. 3a (or Fig. 3b) reveals $v_{r+} = 3.7$ (or 2.8) m s^{-1} and $v_{r-} = 20.7$ (or 21.5) m s^{-1}, so (6) is loosely satisfied. In this case, it is marginally useful to adjust the radial-velocity innovations. As listed in the first column of Table 2, the values of (u^e, v^e) estimated by (8) [or (9)] from dual-Doppler (or single Doppler) radial-velocity innovations are as small as the above values of v_{r+}. This explains why the v_r^{ie} field in Fig. 4a (or Fig. 4b) shows roughly the same pattern as the v_r^i field in Fig. 3a (or Fig. 3b). The solid green zero-v_r^{ie} contour in Fig. 4a (or Fig. 4b), however, becomes notably (or extremely) closer to the estimated vortex center than the solid green zero-v_r^i contour line in Fig. 3a (or Fig. 3b). The dual-Doppler-analyzed vortex wind field from the adjusted radial-velocity innovation data is plotted by the black arrows in Fig. 4c (or Fig. 4d) against the green arrows that replot the vortex wind field in Fig. 4a (or Fig. 4b). As shown in Fig. 4c (or Fig. 4d), the KFDR (or KTLX) single-Doppler-analyzed vortex winds match the dual-Doppler-analyzed vortex winds slightly less well (or notably better) compared to those in Fig. 3c (or Fig. 3d). This explains why the RMSd and RMSd5 values for KFDR (or KTLX) in the last two columns of Table 2 are slightly larger (or notably smaller) than those in the last two columns of Table 1. It is easy to see that each single- or dual-Doppler-analyzed wind field in Fig. 4 is slightly more axisymmetric around the vortex center than its counterpart field in Fig. 3. This may partially explain why the V_{max} values in Table 2 are slightly smaller than their counterpart V_{max} values in Table 1 and thus closer to the V_M values in the first column of Table 1.

The above comparisons suggest that the dual-Doppler analysis in Fig. 4 is slightly more accurate than that in Fig. 3, although the domain-averaged RMS difference between the two dual-Doppler-analyzed total wind fields is merely 0.2 m s^{-1}. For the dual-Doppler analysis in Fig. 4, the total wind field obtained by adding the adjusted background wind field $(u^b, v^b) + (u^e, v^e)$ to the dual-Doppler-analyzed vortex wind field (black arrows in Figs. 4c,d) will be used as a benchmark "truth" to evaluate the total wind fields produced by the stand-alone vortex wind analyses for the same case in the next subsection.

The total wind field produced by the KFDR (or KTLX) single-Doppler analysis in Fig. 4a (or Fig. 4b) is plotted in Fig. 5a (or Fig. 5b) by the color-scaled arrows superimposed on the KFDR (or KTLX) radial-velocity image. The total wind field produced by the dual-Doppler analysis in Fig. 4a is plotted in Fig. 5c by the color-scaled arrows superimposed on the KTLX radial-velocity image. The total wind field in Fig. 5c is replotted by the black arrows in Fig. 5d against the sparse brown arrows for the background wind field (u^b, v^b). As shown, the single-Doppler-analyzed total wind field in either Fig. 5a or 5b reveals nearly the same high-wind (>40 m s^{-1}) areas as the dual-Doppler-analyzed total wind field in Fig. 5c. Similar results are seen for the total wind fields produced by the three analyses in Fig. 3 (without adjusting the background wind). Thus, the total wind field produced by any of the six analyses in Figs. 3 and 4 can be useful or, at least, much more useful than the background wind field for nowcasting the tornadic mesocyclone and associated high-wind areas.

b. *Vortex wind analyses performed in stand-alone fashion*

As explained at the end of section 3a, when the vortex wind analysis is performed in a stand-alone fashion, it is

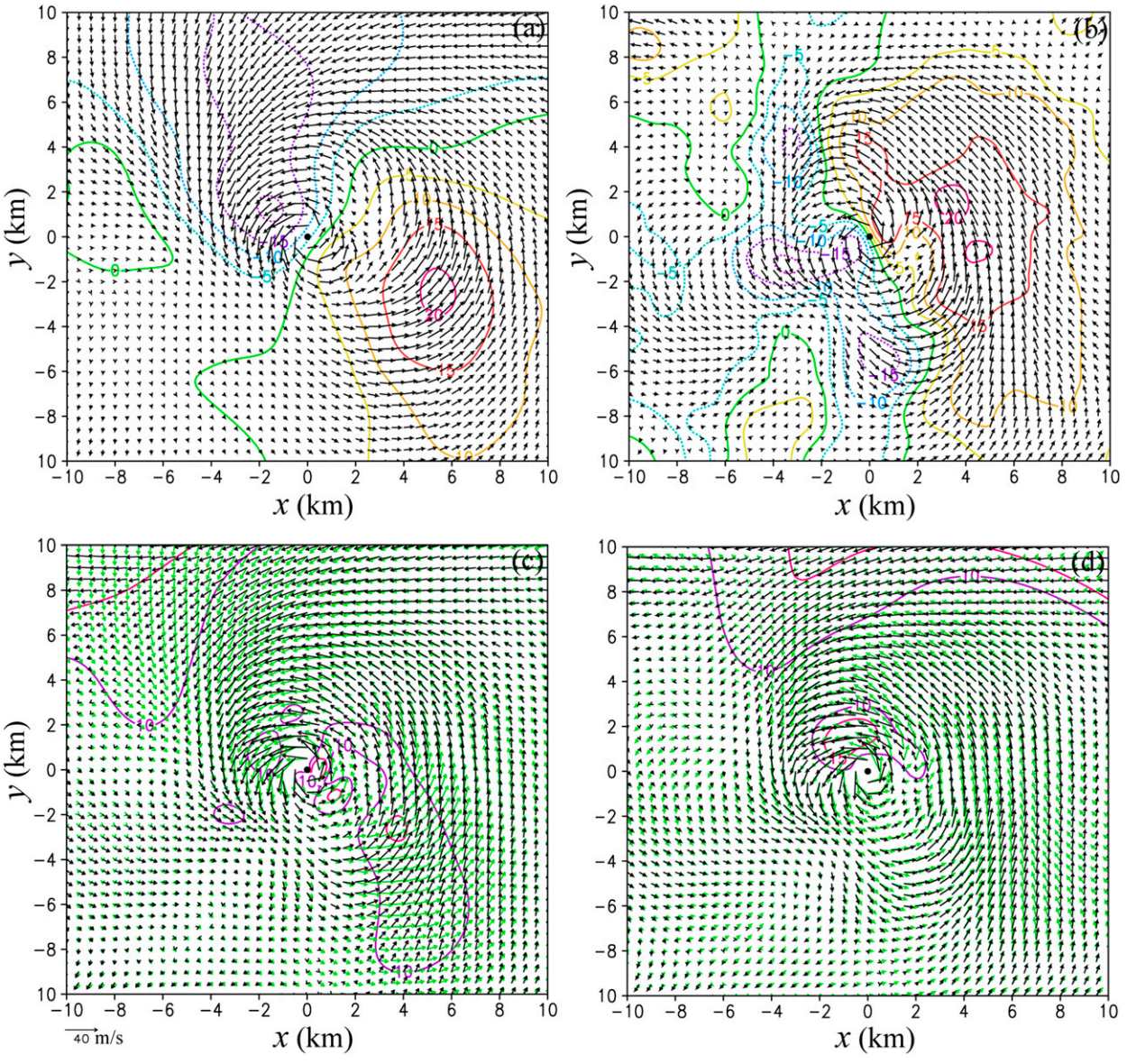

FIG. 4. As in Fig. 3, but for adjusted radial-velocity innovation data [see (10)] in the vortex wind analyses.

necessary to estimate (u^e, v^e) by using (8) [or (9)] from dual-Doppler (or single Doppler) radial-velocity observations. The estimated values of (u^e, v^e) are listed in the first column of Table 3 for the same cases as in the previous subsection. For each case, the estimated (u^e, v^e) is used as a proxy background wind to generate the proxy radial-velocity innovation [still defined as in (5a) except that v_r^b is computed from (u^e, v^e) instead of (u^b, v^b)] at each observation point. The vortex wind field analyzed from the KFDR (or KTLX) proxy radial-velocity innovation data is plotted in Fig. 6a (or Fig. 6b) by the black arrows superimposed on the color contours of the KFDR (or KTLX) proxy radial-velocity innovation field. As shown, the solid green zero-v_r^i contour in Fig. 6a (or Fig. 6b) is slightly off (or extremely close to) the vortex center. This feature is very similar to that for the adjusted radial-velocity innovation field in Fig. 4a (or Fig. 4b).

The vortex wind field analyzed from the dual-Doppler proxy radial-velocity innovation data is plotted by the black arrows in Fig. 6c (or Fig. 6d) against the green arrows that replot the vortex wind field in Fig. 6a (or Fig. 6b). As shown in Fig. 6c (or Fig. 6d), the single-Doppler-analyzed vortex winds match the dual-Doppler-analyzed vortex winds as closely as those in Fig. 4c (or Fig. 4d) over the area of $R \leq 3$ km around the vortex center (or over the entire nested domain), so the single-Doppler analysis can be as useful as the dual-Doppler analysis in terms of extracting the vortex wind field from

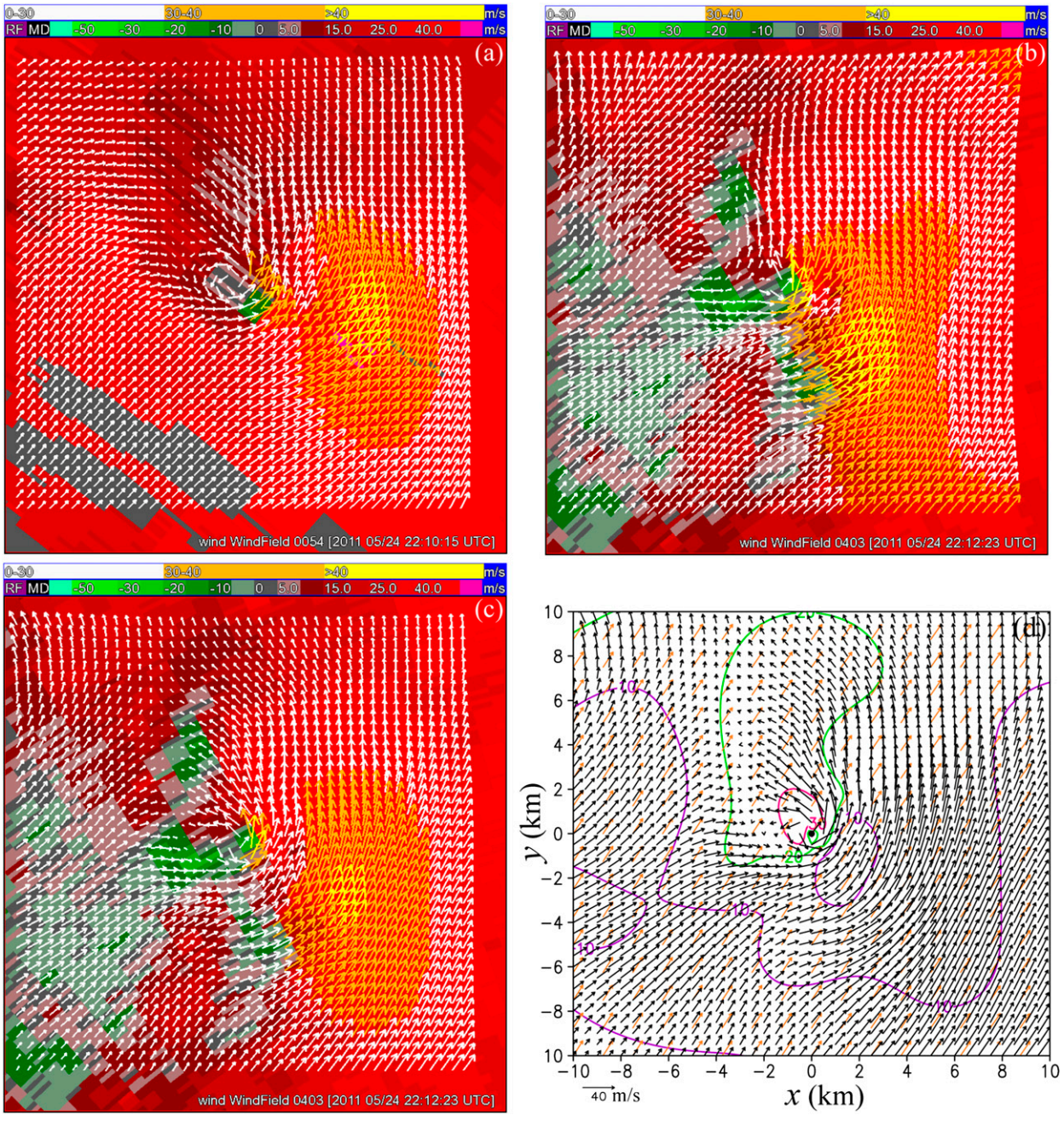

FIG. 5. (a) As in Fig. 4a, but for the total wind field plotted by color-scaled arrows superimposed on the dealiased radial-velocity image from KFDR. (b) As in (a), but for KTLX. (c) As in (b), but for the dual-Doppler-analyzed total wind field. (d) As in (b), but for black arrows plotted together with the background winds (u^b, v^b) plotted by sparse brown arrows superimposed on color contours of the absolute value of the vector difference between the background and dual-Doppler-analyzed winds.

radar radial-velocity observations. However, as shown in the first column of Table 3, the vector value of (u^e, v^e) estimated by (9) from the KFDR (or KTLX) single-Doppler observations is close (or not close) to that estimated by (8) from dual-Doppler observations, and this is simply due to the fact that the KFDR (or KTLX) radar beam is approximately parallel (or perpendicular) to the environmental mean wind estimated by (8) around the vortex. Because of this, the total wind field [i.e., the vortex wind field plus (u^e, v^e)] produced by the KFDR (or KTLX) single-Doppler analysis is slightly (or significantly) less accurate than the total wind field produced by the dual-Doppler analysis. The related RMS errors are listed in the last two columns of

TABLE 3. As in the first three columns of Table 2, but for vortex wind analyses using the proxy background winds (listed in the first column). In the fourth (or fifth) column, RMSE (or RMSE5) is the RMS error of the analyzed total wind field evaluated against the benchmark truth total wind field in Fig. 4c over the nested domain (or within $R \leq 5$ km from the vortex center).

Radar	(u^e, v^e) (m s^{-1})	V_{max} (m s^{-1})	R_{max} (km)	RMSE (m s^{-1})	RMSE5 (m s^{-1})
KFDR	(15.7, 19.9)	36.1	0.90	10.5	10.1
KTLX	(−6.5, 12.1)	33.2	0.56	16.9	15.8
KTLX and KFDR	(12.6, 22.3)	36.1	0.71	9.2	7.8

Table 3, where RMSE (or RMSE5) is the RMS error of the total wind field evaluated against the benchmark truth total wind field in Fig. 4c over the nested domain (or within $R \leq 5$ km from the vortex center).

As indicated by the results in Fig. 6 and Table 3, the stand-alone single-Doppler analysis can reliably extract the vortex wind field but cannot reliably capture the high-wind areas in the total wind field if (u^e, v^e) is poorly

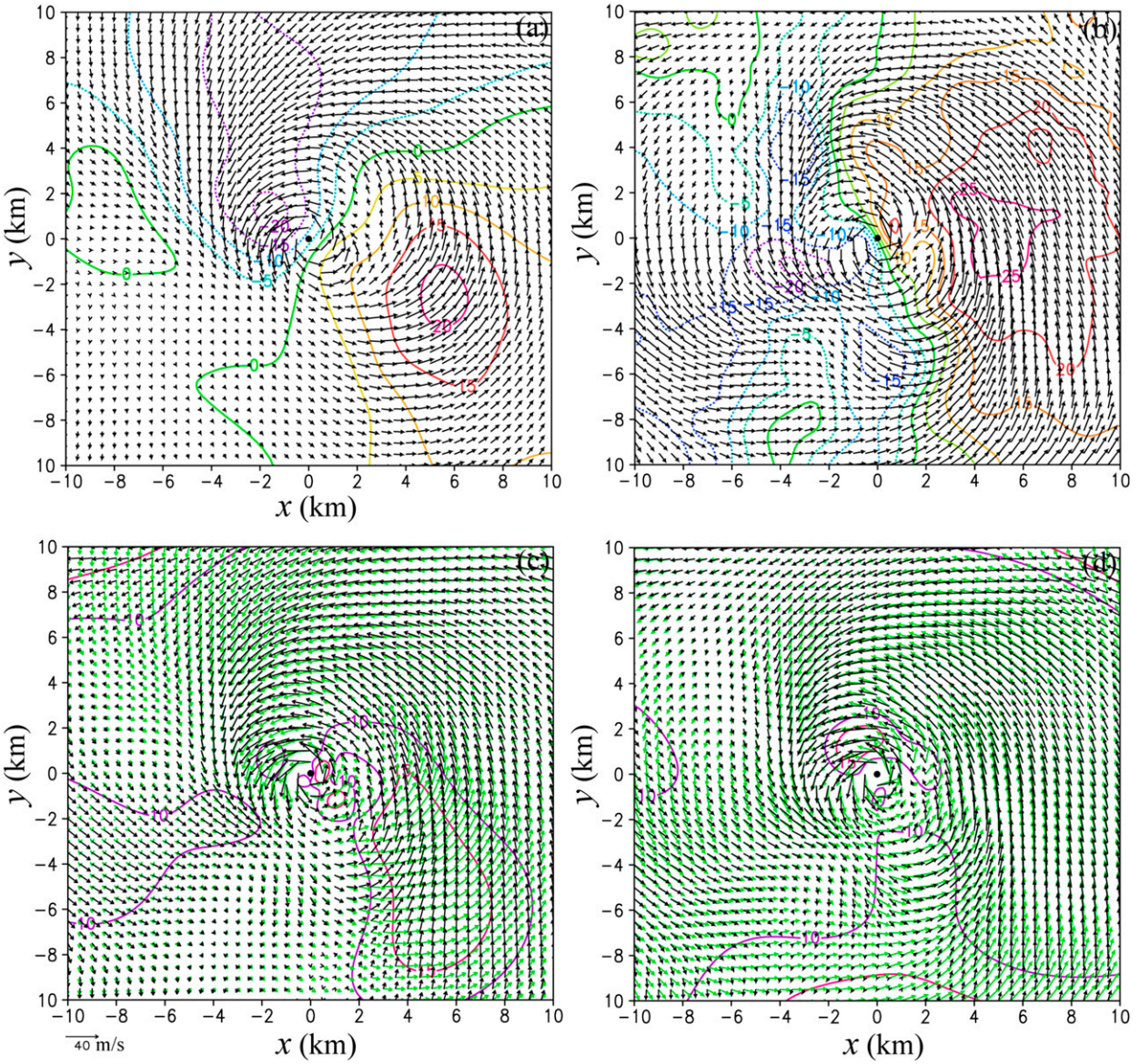

FIG. 6. As in Fig. 3, but for the stand-alone analyses that use the proxy background winds listed in the first column of Table 3 in place of the RWAS-produced background wind field.

estimated in (9). In this case, as explained earlier [see the text following (9)], the vortex center moving velocity (u^c, v^c) estimated by the time change rate of the vortex center location on the same tilt from the previous to the current volume scan can be used as a proxy background wind for the single-Doppler vortex wind analysis. The estimated value is $(u^c, v^c) = (17.6, 9.3)\ \mathrm{m\,s^{-1}}$ for KTLX, and this vector value is closer to the dual-Doppler-estimated value of $(u^e, v^e) = (12.6, 22.3)\ \mathrm{m\,s^{-1}}$ than the KLTX single-Doppler-estimated value of $(u^e, v^e) = (-6.5, 12.1)\ \mathrm{m\,s^{-1}}$ in Table 3. When this estimated (u^c, v^c) is used as a proxy background wind, the RMSE (or RMSE5) reduces from 16.9 (or 15.8) $\mathrm{m\,s^{-1}}$ to 11.6 (or 10.9) $\mathrm{m\,s^{-1}}$ for the KTLX single-Doppler-analyzed total wind field.

The stand-alone single-Doppler analysis has also been applied to the KTLX radial-velocity scans of the tornadic mesocyclone and its produced tornado, which was rated as category 5 on the enhanced Fujita scale (EF5). The tornado struck the cities of Newcastle and Moore, Oklahoma, in the afternoon (between 1445 and 1535 local time) on 20 May 2013. As an example, the analyzed vortex wind field is plotted in Fig. 7a by the black arrows superimposed on the color contours of the proxy radial-velocity innovation field computed from the KTLX radial-velocity observations at 0.5° tilt (around z = 0.67 km) at 2008:42 UTC. The estimated vortex center is at $(r_c, \varphi_c) = (28.875\ \mathrm{km}, 266°)$ in the KTLX coordinates, and this estimated vortex center is very close to the solid green zero-v_r^i contour in Fig. 7a. As listed in the first column of Table 4, the environmental mean wind estimated by (9) from KTLX single-Doppler observations is $(u^e, v^e) = (8.0, 0.6)\ \mathrm{m\,s^{-1}}$, which is quite close to the vortex center moving velocity of $(u^c, v^c) = (7.3, 3.3)\ \mathrm{m\,s^{-1}}$ estimated by the time change rate of vortex center location at 0.5° tilt. The $V_{\max}$ (or $R_{\max}$) value listed in the fourth (or fifth) column of Table 4 for the vortex wind field in Fig. 7a is close to the V_M (or R_M) value estimated from the KTLX radial-velocity observations in the second (or third) column of Table 4.

The total wind field [i.e., the vortex wind field in Fig. 7a plus the proxy background wind (u^e, v^e)] is shown in Fig. 7b by the color-scaled arrows superimposed on the KTLX radial-velocity image. As shown, the winds were strongest in a small area immediately to south and southeast of the vortex center and this high-wind area was moving with the tornadic mesocyclone toward Moore. Assuming that the above-estimated vortex center moving velocity of $(u^c, v^c) = (7.3, 3.3)\ \mathrm{m\,s^{-1}}$ represents the environmental mean wind more accurately than the single-Doppler-estimated (u^e, v^e) in Table 4, the total wind field (not shown) produced by using (u^c, v^c) [instead of (u^e, v^e)] as the proxy background wind can be used as a benchmark

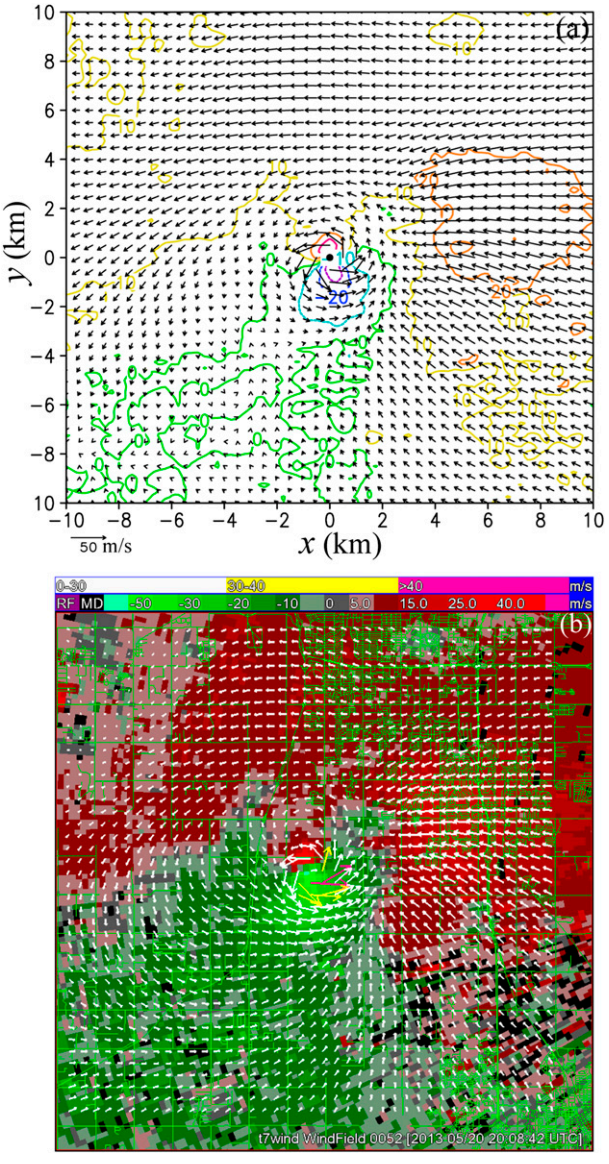

FIG. 7. (a) Stand-alone single-Doppler-analyzed vortex winds plotted by black arrows superimposed on the color contours of the proxy radial-velocity innovation field from KTLX at 0.5° tilt (around z = 0.67 km) for the tornadic mesocyclone at 2008:42 UTC 20 May 2013. (b) Single-Doppler-analyzed total wind field plotted by color-scaled arrows superimposed on the radial-velocity image from KTLX for the same case as in (a). The thin green lines in (b) show the county boundaries and the streets of Moore. KTLX is located at $(x, y) = (28.80, -2.01)$ km outside the analysis domain.

truth to evaluate the error of the total wind field in Fig. 7b. As listed in the last two columns of Table 4, the evaluated RMS error is RMSE = 2.6 (or RMSE5 = 2.7) $\mathrm{m\,s^{-1}}$ over the nested domain (or within $R \le 5$ km from the vortex center). Note that the environment winds around the mesocyclone were largely toward KTLX, so (u^e, v^e) can be well estimated by (9). This explains why

TABLE 4. As in Table 3, but for the single-Doppler vortex wind analysis of the tornadic mesocyclone scanned by KTLX at 0.5° tilt at 2008:42 UTC 20 May 2013. Here, RMSE (or RMSE5) is the RMS error of the total wind field in Fig. 7b evaluated over the nested domain (or within $R \leq 5$ km from the vortex center) against the benchmark truth total wind field obtained by the same single-Doppler vortex wind analysis but using (u^c, v^c) instead of (u^e, v^e) as the proxy background wind.

Radar	(u^e, v^e) (m s^{-1})	V_M (m s^{-1})	R_M (km)	$V_{\max}$ (m s^{-1})	$R_{\max}$ (km)	RMSE (m s^{-1})	RMSE5 (m s^{-1})
KTLX	(8.0, 0.6)	45.0	0.46	40.3	0.50	2.6	2.7

$(u^e, v^e) \approx (u^c, v^c)$ and why RMSE and RMSE5 are quite small, as shown in Table 4.

5. Conclusions

In this paper, a new method is developed for analyzing the vortex wind fields from radar-observed mesocyclones. The method contains three key components. The first component is an automated algorithm for estimating the vortex center of the mesocyclone (detected as a by-product of Doppler velocity dealiasing) on a selected tilt of a radar scan. The second component is a vortex-flow-dependent background error correlation function formulated in the cylindrical coordinates cocentered with the mesocyclone for the vortex wind analysis on the selected tilt. The third component is the square root of the vortex-flow-dependent background error covariance matrix derived analytically to precondition the cost function and enhance the computational efficiency.

The method is incorporated into the existing radar wind analysis system (RWAS; Xu et al. 2015) as an additional (fourth) step of targeted finescale analysis after the third step is performed in the RWAS. The method can be also used in a stand-alone fashion, but this stand-alone application requires the environmental mean wind to be estimated around the vortex and used as a proxy background wind.

The effectiveness and performance of the method are demonstrated by examples of analyzed vortex wind fields and total wind fields for the Oklahoma tornadic mesocyclones observed by KFDR and KTLX on 24 May 2011 and by KTLX on 20 May 2013. The results are summarized below.

1) When the method is used with the RWAS-produced background wind field, the single-Doppler-analyzed vortex wind field can match the gross pattern of the dual-Doppler-analyzed vortex wind field and the RMS difference between the two analyzed fields ranges from 7.1 to 8.6 m s^{-1} (see Fig. 3 and Table 1). Estimating the environmental mean wind around the vortex atop the RWAS-produced background wind field [see (8) and (9)] and using it to adjust the background wind field and thus the radial-velocity innovation data [see (10)] may only slightly improve the vortex wind analyses (see Fig. 4 and Table 2).
2) When the RWAS-produced background wind field or the adjusted background wind field is used, the total wind field produced by either single-Doppler or dual-Doppler analysis can be useful or, at least, much more useful than the RWAS-produced background wind field for nowcasting the tornadic mesocyclone and associated high-wind areas (see Fig. 5).
3) When the method is used in stand-alone fashion, it is necessary to use the estimated environmental mean wind around the vortex as a proxy background wind for the vortex wind analysis. In this case, although the analyzed vortex wind field is not very sensitive to the estimated environmental mean wind (see Fig. 6), the accuracy of the analyzed total wind field depends on the accuracy of the estimated environmental mean wind (see Tables 3 and 4).
4) The environmental mean wind can be estimated reliably from dual-Doppler radial-velocity observations [see (8)] but not reliably from single-Doppler radial-velocity observations [see (9)]. For the single-Doppler case, the vortex center moving velocity (estimated by the time change of the vortex center location from the previous to the current volume scan) can be used as a proxy background wind for the stand-alone single-Doppler vortex wind analysis. With a reliably estimated proxy background wind, the total wind field produced by the stand-alone single-Doppler analysis can be useful for nowcasting the tornadic mesocyclone and associated high-wind areas (see Fig. 7).

The consistency and stability of the method can be further examined and have been well verified by applying the method to consecutive data volumes for the two cases considered in this paper, but the detailed results are omitted. In summary, the method is computationally very efficient and it can retrieve the vortex part of the mesocyclone winds from merely single-Doppler observations. These are the strengths of the method. The method is expected to work best when the mesocyclone is intense and not too far (within 100 km) from the radar, and this is another strength of the method. On the other hand, the method may not work well when the mesocyclone is small and far from the radar where the radar beam becomes wider than the vortex core diameter. In addition, the method may not accurately

retrieve the total wind field when the environmental mean wind cannot be reliably estimated from a single-Doppler volume scan in the stand-alone application. These are the weaknesses of the method. The vortex moving velocity may be used as a proxy background wind for the stand-alone application, but how to accurately estimate the vortex center moving velocity requires further investigation.

Since the multifunction phased-array radar (PAR) technology is under consideration for future operational weather radars (Zrnic et al. 2007), we will also use the PAR data to evaluate the performances of the method developed in this paper. The method can be extended to analyze three-dimensional vortex winds in Cartesian coordinates from either single- or multi-Doppler scans of mesocyclones with the background wind error correction functions formulated in a slantwise cylindrical coordinate system cocentered with the mesocyclone at each vertical level. This capability is currently being developed.

Acknowledgments. The authors are thankful to the anonymous reviewers, Vincent Wood, and Travis Smith of NSSL for their comments and suggestions that improved the presentation of the paper. The research was supported by ONR Grant N000141410281 to the University of Oklahoma (OU). Funding was also provided to CIMMS by NOAA/Office of Oceanic and Atmospheric Research under NOAA–OU Cooperative Agreement NA11OAR4320072, U.S. Department of Commerce.

REFERENCES

Daley, R., 1991: *Atmospheric Data Analysis*. Cambridge University Press, 457 pp.

Doviak, R. J., and D. S. Zrnic, 2006: *Doppler Radar and Weather Observations*. 2nd ed. Dover, 562 pp.

Fast, J. D., R. K. Newsom, K. J. Allwine, Q. Xu, P. Zhang, J. Copeland, and J. Sun, 2008: An evaluation of two NEXRAD wind retrieval methodologies and their use in atmospheric dispersion models. *J. Appl. Meteor. Climatol.*, **47**, 2351–2371, doi:10.1175/2008JAMC1853.1.

Gao, J., and Coauthors, 2013: A real-time weather-adaptive 3DVAR analysis system for severe weather detections and warnings. *Wea. Forecasting*, **28**, 727–745, doi:10.1175/WAF-D-12-00093.1.

Liu, S., M. Xue, and Q. Xu, 2007: Using wavelet analysis to detect tornadoes from Doppler radar radial-velocity observations. *J. Atmos. Oceanic Technol.*, **24**, 344–359, doi:10.1175/JTECH1989.1.

Lu, H., Q. Xu, M. Yao, and S. Gao, 2011: Time-expanded sampling for ensemble-based filters: Assimilation experiments with real radar observations. *Adv. Atmos. Sci.*, **28**, 743–757, doi:10.1007/s00376-010-0021-4.

Miller, M. L., V. Lakshmanan, and T. M. Smith, 2013: An automated method for depicting mesocyclone paths and intensities. *Wea. Forecasting*, **28**, 570–585, doi:10.1175/WAF-D-12-00065.1.

Newman, J. F., V. Lakshmanan, P. L. Heinselman, M. B. Richman, and T. M. Smith, 2013: Range-correcting azimuthal shear in Doppler radar data. *Wea. Forecasting*, **28**, 194–211, doi:10.1175/WAF-D-11-00154.1.

Newsom, R. K., and Coauthors, 2014: Evaluation of single-Doppler radar wind retrievals in flat and complex terrain. *J. Appl. Meteor. Climatol.*, **53**, 1920–1931, doi:10.1175/JAMC-D-13-0297.1.

Potvin, C. K., A. Shapiro, T.-Y. Yu, J. Gao, and M. Xue, 2009: Using a low-order model to detect and characterize tornadoes in multiple-Doppler radar data. *Mon. Wea. Rev.*, **137**, 1230–1249, doi:10.1175/2008MWR2446.1.

——, ——, M. I. Biggerstaff, and J. M. Wurman, 2011: The VDAC technique: A variational method for detecting and characterizing convective vortices in multiple-Doppler radar data. *Mon. Wea. Rev.*, **139**, 2593–2613, doi:10.1175/2011MWR3638.1.

Smith, T. M., and K. L. Elmore, 2004: The use of radial velocity derivatives to diagnose rotation and divergence. Preprints, *11th Conf. on Aviation, Range, and Aerospace*, Hyannis, MA, Amer. Meteor. Soc., P5.6. [Available https://ams.confex.com/ams/pdfpapers/81827.pdf.]

Stumpf, G. J., A. Witt, E. D. Mitchell, P. L. Spencer, J. T. Johnson, M. D. Eilts, K. W. Thomas, and D. W. Burgess, 1998: The National Severe Storms Laboratory mesocyclone detection algorithm for the WSR-88D. *Wea. Forecasting*, **13**, 304–326, doi:10.1175/1520-0434(1998)013<0304:TNSSLM>2.0.CO;2.

Wood, V. T., and R. A. Brown, 1992: Effects of radar proximity on single-Doppler velocity signatures of axisymmetric rotation and divergence. *Mon. Wea. Rev.*, **120**, 2798–2807, doi:10.1175/1520-0493(1992)120<2798:EORPOS>2.0.CO;2.

Xu, Q., 2011: Measuring information content from observations for data assimilation: Spectral formulations and their implications to observational data compression. *Tellus*, **63A**, 793–804, doi:10.1111/j.1600-0870.2011.00524.x.

——, and L. Wei, 2011: Measuring information content from observations for data assimilation: Utilities of spectral formulations for radar data compression. *Tellus*, **63A**, 1014–1027, doi:10.1111/j.1600-0870.2011.00542.x.

——, and ——, 2013: Prognostic equation for radar radial velocity derived by considering atmospheric refraction and Earth curvature. *J. Atmos. Sci.*, **70**, 3328–3338, doi:10.1175/JAS-D-13-011.1.

——, K. Nai, and L. Wei, 2007: An innovation method for estimating radar radial-velocity observation error and background wind error covariances. *Quart. J. Roy. Meteor. Soc.*, **133**, 407–415, doi:10.1002/qj.21.

——, ——, ——, P. Zhang, S. Liu, and D. Parrish, 2011: A VAD-based dealiasing method for radar velocity data quality control. *J. Atmos. Oceanic Technol.*, **28**, 50–62, doi:10.1175/2010JTECHA1444.1.

——, ——, S. Liu, C. Karstens, T. Smith, and Q. Zhao, 2013: Improved Doppler velocity dealiasing for radar data assimilation and storm-scale vortex detection. *Adv. Meteor.*, **2013**, 562386, doi:10.1155/2013/562386.

——, L. Wei, K. Nai, S. Liu, R. M. Rabin, and Q. Zhao, 2015: A radar wind analysis system for nowcast applications. *Adv. Meteor.*, **2015**, 264515, doi:10.1155/2015/264515.

Zrnic, D. S., and Coauthors, 2007: Agile-beam phased array radar for weather observations. *Bull. Amer. Meteor. Soc.*, **88**, 1753–1766, doi:10.1175/BAMS-88-11-1753.